Title

Compatibility of internal transport barrier with steady-state operation in the high bootstrap fraction regime on DIII-D

Permalink

https://escholarship.org/uc/item/9rp7k3pk

Journal

Nuclear Fusion, 55(12)

ISSN

0029-5515

Authors

Garofalo, AM
Gong, X
Grierson, BA
et al.

Publication Date

2015-11-16

DOI

10.1088/0029-5515/55/12/123025

Peer reviewed

Compatibility of internal transport barrier with steady-state operation in the high bootstrap fraction regime on DIII-D

A.M. Garofalo[1]**, X. Gong**[2]**, B.A. Grierson**[3]**, Q. Ren**[2]**, W.M. Solomon**[3]**,**
E.J. Strait[1]**, M.A. Van Zeeland**[1]**, C.T. Holcomb**[4]**, O. Meneghini**[1]**, S.P. Smith**[1]**,**
G.M. Staebler[1]**, B. Wan**[2]**, R. Bravenec**[5]**, R.V. Budny**[3]**, S. Ding**[2]**, J.M. Hanson**[6]**,**
W.W. Heidbrink[7]**, L.L. Lao**[1]**, G. Li**[2]**, C. Pan**[2]**, C.C. Petty**[1]**, J. Qian**[2]**,**
C. Paz-Soldan[1]** and G. Xu**[2]

[1] General Atomics, PO Box 85608, San Diego, CA 92186–5608, USA
[2] Institute of Plasma Physics Chinese Academy of Sciences, 350 Shushanhu Rd, Hefei, Anhui 230031, People's Republic of China
[3] Princeton Plasma Physics Laboratory, PO Box 451, Princeton, NJ 08543-0451, USA
[4] Lawrence Livermore National Laboratory, 7000 East Ave, Livermore, CA 94550, USA
[5] Fourth State Research, 503 Lockhart Dr., Austin, TX 78704, USA
[6] Columbia University, 116th St and Broadway, New York, NY 10027–6900, USA
[7] University of California Irvine, University Dr., Irvine, CA92697, USA

E-mail: garofalo@fusion.gat.com

CrossMark

Abstract

Recent EAST/DIII-D joint experiments on the high poloidal beta tokamak regime in DIII-D have demonstrated fully noninductive operation with an internal transport barrier (ITB) at large minor radius, at normalized fusion performance increased by $\geqslant 30\%$ relative to earlier work (Politzer *et al* 2005 *Nucl. Fusion* **45** 417). The advancement was enabled by improved understanding of the 'relaxation oscillations', previously attributed to repetitive ITB collapses, and of the fast ion behavior in this regime. It was found that the 'relaxation oscillations' are coupled core-edge modes amenable to wall-stabilization, and that fast ion losses which previously dictated a large plasma-wall separation to avoid wall over-heating, can be reduced to classical levels with sufficient plasma density. By using optimized waveforms of the plasma-wall separation and plasma density, fully noninductive plasmas have been sustained for long durations with excellent energy confinement quality, bootstrap fraction $\geqslant 80\%$, $\beta_N \leqslant 4$, $\beta_P \geqslant 3$, and $\beta_T \geqslant 2\%$. These results bolster the applicability of the high poloidal beta tokamak regime toward the realization of a steady-state fusion reactor.

Keywords: steady state, ion transport barrier, wall stabilization, high beta

(Some figures may appear in colour only in the online journal)

1. Introduction

A high bootstrap current fraction plasma regime is desirable for steady-state tokamak operation because it reduces the demands on external noninductive current drive. The bootstrap current fraction, f_{BS}, is proportional to the poloidal beta, $\beta_p = \beta_T \times \left(\frac{B_T}{B_P} \right)^2$, where $\beta_T = p/(B_T^2/2\mu_0)$ is the dimensionless plasma pressure, and B_T and B_P are the toroidal and poloidal magnetic field strengths. Often, this regime is characterized by high β_N [$\beta_N = \beta_T/(I_P/aB_T)$, with I_p the toroidal plasma current and a the plasma minor radius] and an internal transport barrier (ITB), leading to concerns about β_N stability limits and profile control with reduced external input (power). Recent DIII-D research has increased confidence in the potential of the high

bootstrap fraction approach for applicability to a steady-state fusion reactor. This effort was largely motivated by the interest in developing and testing a possible scenario for steady-state advanced tokamak demonstration on EAST [1]. Building on earlier JT-60U [2–4] and DIII-D [5] work, a joint team of scientists from DIII-D and EAST adopted an approach to fully noninductive operation based on high β_P ($\beta_P \geqslant 3$) operation without the current drive by transformer induction. Utilizing new DIII-D capabilities and diagnostics with improved time and spatial resolutions, these experiments have led to increased physics understanding of the performance limitations, and ultimately to increased plasma performance.

Experiments on JT-60U [2, 3] had demonstrated near fully non-inductive high bootstrap current fraction discharges with large ITB radius, showing that larger ITB radius was obtained with larger f_{BS}. High confinement could be sustained in negative central magnetic shear (NCS) plasmas for durations much longer that the current diffusion time as long as a large $\rho(q_{min})$ could be sustained by noninductive (bootstrap or external) current drive. Although low I_p (0.8 MA) high q operation ($q_{95} \approx 9$) was necessary to sustain large $\rho(q_{min})$ with the current drive capabilities of JT-60U, that research suggested that steady-state high confinement NCS plasmas could be obtained in a lower q and higher β_T regime with more off-axis current drive power. The maximum β_N achieved in these JT-60U experiments was limited to about 2.

Taking advantage of wall-stabilization [6, 7], high β_P experiments achieved higher β_N. On JT-60U [4] the maximum β_N was increased to ~2.7, very close to the calculated ideal wall limit ~2.9. Similarly, experiments on DIII-D achieved $\beta_N \sim 3$, $\beta_P \sim 3$ and $\beta_T \sim 1.5\%$ with $q_{min} \sim 3$ and $q_{95} \sim 11$ [5]. To address reactor relevant issues of control near the beta limit in fully noninductive conditions with very high bootstrap fraction, these DIII-D experiments clamped the current in the transformer coil after the current flattop was reached. The achievable plasma current and pressure were limited by a relaxation oscillation, described as the repetitive buildup and collapse of an ITB at large minor radius. These relaxation oscillations were attributed to a misalignment between the bootstrap and the externally driven non-inductive current densities [8].

In the recent DIII-D experiments, fully noninductive plasmas have been sustained for long durations with $f_{BS} \geqslant 80\%$ and large-radius ITBs, at normalized fusion performance increased by $\geqslant 30\%$ relative to the earlier DIII-D work [5]. The advancement was enabled by improved understanding of the 'relaxation oscillations' and the fast ion behavior in this regime. Relaxation oscillations are observed to limit the plasma performance in these experiments as well, but the main cause is identified as the $n = 1$ ideal-wall external kink mode, causing a repetitive collapse of the H-mode pedestal, not the ITB. The $n = 1$ external kink mode is found to be close to the ideal-wall limit at $\beta_N \sim 3$ with a plasma-wall separation similar to the earlier experiments [5]. This plasma-wall separation is larger than usual for DIII-D experiments, and was deemed necessary to avoid wall over-heating by fast ion losses in this low plasma current regime. However, in the course of the work described in this paper, it was found that fast ion losses can be reduced to classical levels with sufficient plasma
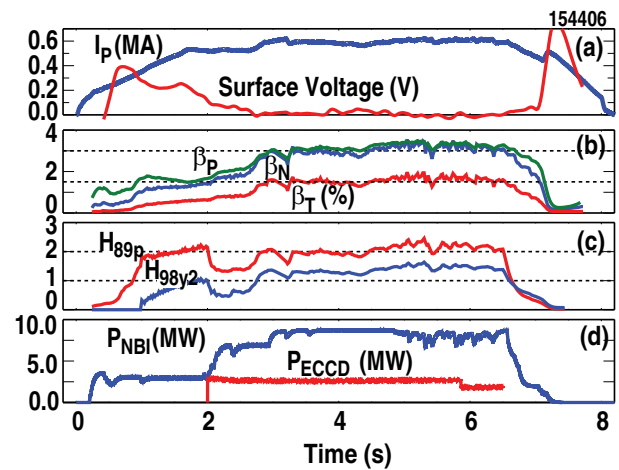

Figure 1. Time traces of selected plasma parameters for representative high β_P discharge 154 406.

density. The new understanding of relaxation oscillations and fast ion losses in the high β_P regime on DIII-D was tested by using optimized waveforms of the plasma-wall separation and plasma density, and resulted in the extension of the plasma performance to $\beta_N \approx \beta_P \sim 4$, and $\beta_T \geqslant 2\%$.

The remainder of the paper is organized as follows: section 2 presents current profile and transport analysis, discussing in particular the issue of E × B shear effects on the bootstrap current alignment. Section 3 investigates ideal MHD stability and fast ion losses. Section 4 describes the new understanding of the performance limiting instabilities, showing that ITBs can be compatible with steady-state operation at beta within the $n = 1$ ideal-wall limit, and leading to new experiments with improved plasma performance. Section 5 summarizes the results and illustrates how the normalized fusion performance of these high bootstrap current fraction plasmas is comparable to the targets of design studies for economical steady-state fusion reactors.

2. Fully noninductive operation

Figure 1 shows time histories of several plasma parameters for a representative fully noninductive, high β_P discharge with performance similar to the previous DIII-D results. The plasma cross section is an upper-biased double-null divertor shape [i.e. with up-down symmetry slightly broken to favor formation of the upper x-point, as shown in figure 5(*a*)], with elongation $\kappa \sim 1.86$ and average triangularity (top and bottom) 0.6. The toroidal field is $\beta_T = 2T$. After an approximate equilibrium is established (1.7 s) the current in the transformer coil is fixed, so that the plasma current is forced to relax noninductively. A flattop at approximately 0.6 MA is achieved by an appropriate programming of the β_N waveform, which is feedback controlled using neutral beam power. This waveform was obtained by increasing from shot to shot the reference β_N, thus increasing the bootstrap current fraction, until the plasma current became constant. The plasma current is maintained in 100% noninductive condition, as shown by the ~zero surface voltage signal, for the rest of the discharge
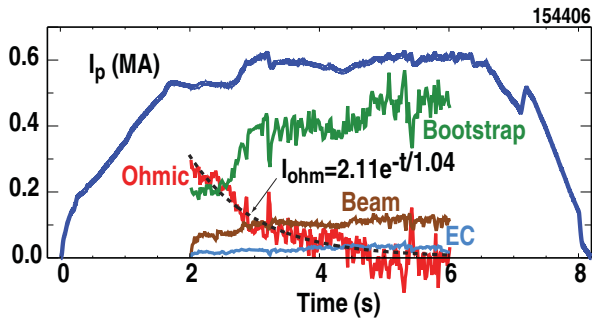
Figure 2. Time traces of total plasma current I_P (blue) and its components: bootstrap (green), beam driven (brown), EC driven (azul), and Ohmic (red). Dashed black line is the exponential fit of the Ohmic component. Spikes in the traces are due to the relaxation oscillations, discussed in section 4. Discharge 154 406.

Figure 3. Radial profiles for discharge 154 406 at $t = 5.17$ s, showing ITB at $\rho \sim 0.7$: (*a*) Ion and electron temperature, (*b*) rotation (of carbon impurity ions) and electron density, (*c*) pressure and safety factor, (*d*) plasma current density (total, ECCD, NBI driven, and bootstrap according to the NEO and Sauter models). Vertical dashed line across panels (*a*) and (*b*) marks the foot of the ITB in the rotation profile.

duration, limited by hardware constraints on DIII-D pulse length.

This discharge achieves and maintains $\beta_N \sim \beta_P \gtrsim 3$ and $\beta_T \sim 1.5\%$, with about 20% non-thermal fraction of β and Greenwald density fraction $f_{GW} \gtrsim 0.9$, using a total heating and current drive power of ~11 MW. This power includes ~3.5 MW of on-axis neutral beam injection (NBI), ~5 MW of off-axis ($\rho \sim 0.4$) NBI, and 2.5 MW of off-axis electron cyclotron current drive (ECCD), injected at $\rho \sim 0.5$.

The various current components for discharge 154406, plotted in figure 2, are calculated from experimental profiles by the TRANSP code [9]. The bootstrap current fraction reaches up to 80%–85%, the NBI-driven current fraction is 15%–20%, and only <5% of the total current is driven by EC frequency electromagnetic waves, since the efficiency of ECCD is low at large minor radius. Note that despite having the transformer coil current clamped, some loop voltage may be driven by current variations in the shaping and vertical field coils. An exponential fit to the calculated Ohmic current yields a time constant of ~1.06 s. This is in close agreement with the current profile relaxation time estimated as $\tau_{CR} = 0.17 * R/\text{Resistance} = 1 - 2\text{s}$ [10], evaluated between 2 and 6 s in this discharge, therefore supporting that the plasma current is indeed relaxing noninductively.

This plasma exhibits excellent energy confinement quality, with confinement enhancement factor over H-mode confinement scaling $H_{98y,2}$ up to ~1.5. The exceeding of $H_{98y,2} \sim 1$ is associated with the formation of an ITB at large minor radius ($\rho \sim 0.7$) in all channels (n_e, T_e, T_i rotation), shown in figures 3(*a*) and (*b*). Note how the ITB in the ion temperature is not very steep. Steeper T_i ITBs and weaker T_e ITBs are observed in cases without ECCD. Good alignment of the bootstrap and total current profiles, shown in figure 3(*d*), enables sustainment of the large radius ITB. In this figure, the current profile is from an EFIT [11] equilibrium reconstruction including kinetic and MSE measurements, and using the bootstrap current predicted by the first principle kinetic code NEO [12] to further constrain the edge current density at minor radius $0.8 < \rho < 1$, a reasonable approach since the analysis time is more than two current profile relaxation times after the clamping of the transformer coil. As an indication of the uncertainty in the determination of the current profile
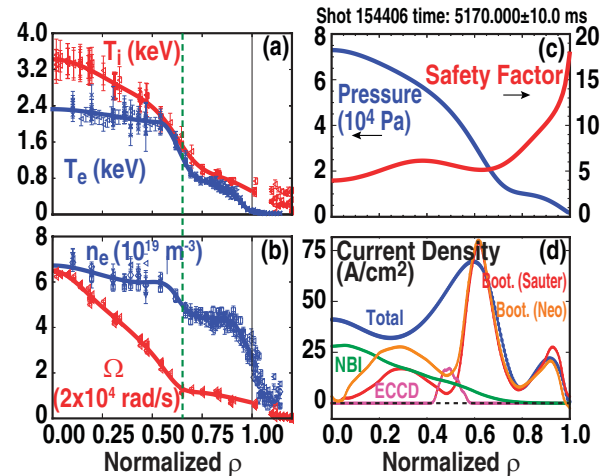
components, the bootstrap current calculated using the Sauter model [13] is also shown. Constraining the edge current density using the Sauter model is also consistent with the experimental measurements. Small pockets of Ohmic current (both negative and positive) may be inferred at various radii. These may be real, due for example to the large relaxation oscillations in this discharge, or simply an artifact of the limited accuracy of the current profile reconstruction.

Figure 3(*c*) shows the pressure and *q*-profiles. Note that the *q*-profile does not necessarily show an absolute minimum near the location of the ITB. In many cases, similar to discharge 154406, the *q*-profile is near monotonic, with a local minimum at $\rho \sim 0.6$, similar to what was reported previously [5]. However, no adverse or beneficial effect has been observed in cases where, due to stronger early heating, the *q*-profile develops strong shear reversal in the core, with very high central safety factor $q_0 \sim 10$ maintained throughout the discharge. Also, sustainment of the ITB at a large radius is not tied to the use of off-axis external current drive. Sustained high q_{min} and large radius ITB are observed with off-axis NBI (figure 1) or without off-axis NBI {previous work [5]}, and with or without off-axis ECCD, {as also reported in [5]}.

The good alignment of the bootstrap current with respect to the total current density profile in figure 3(*d*) is obtained with an ITB that extends into regions of positive magnetic shear, i.e. minor radius > local minimum at $\rho \sim 0.6$. ITBs which only exist at minor radius < local (or absolute) minimum, generate a peak in the bootstrap current profile at a smaller radius than is required for alignment with the peak in the total current density profile, resulting in a progressive shrinking of the ITB radius {see, for example, [14, 15]}. The observation of ITBs extending into the positive magnetic shear region has been made on several tokamaks, with monotonic *q*-profiles such as in [16, 17]; and in *q*-profiles with strong shear reversal in the core, such as in [2]. On JET, it was argued by Tala *et al* [18] that

essential to these type of ITBs is the presence of high values of rotational shear, raising questions concerning the relevance of ITBs in the positive magnetic shear region to future devices where rotation effects are likely to be smaller than in present tokamaks (at least those with unbalanced NBI). However, in these high-β_P discharges the ITB foot in the rotation profile is observed at smaller minor radius than in all other profiles, as shown by the vertical dashed line in figures 3(*a*) and (*b*). This suggests that shear in the toroidal rotation is not critical to the formation of the ITB. Transport analysis can address this issue in a more quantitative manner.

Here, transport modeling is carried out using the code TGYRO [19], which can predict the plasma profiles combining turbulent particle and energy fluxes from TGLF [20] and the neoclassical fluxes from NEO [12]. TGLF is a quasi-linear transport model that uses a reduced gyro-fluid system of moments of the linear gyrokinetic equation to compute the spectrum of linear eigenmode instabilities. Adding the turbulent transport from TGLF to the neoclassical transport from NEO has proven to be an accurate predictive theory-based transport model for the core of L-mode and H-mode inductive discharges and DIII-D hybrid regimes [21]. However, very high-β_P discharges push into plasma conditions that are quite different from the discharges where TGLF plus NEO have been successful at predicting transport, and quite different from the standard case used to calibrate [21] the TGLF electron energy transport due to ETG modes to full gyrokinetic nonlinear simulations using GYRO [22]. A key difference may be the fact that the safety factor profile is much higher (at all radii) in the high-β_P cases. Indeed, in simulations of high-β_P discharges where both the electron and ion temperature profiles are evolved, the predicted profiles from TGYRO differ significantly from the experimental profiles. In particular, the electron temperature profile is generally over-predicted by more than a factor of two. The reasons for this discrepancy are currently being investigated.

On the other hand, if the electron profile is kept fixed, simulations (including self-consistent ion–electron exchange terms) are consistently able to accurately reproduce the ion temperature profile. An example of these transport simulations is shown in figure 4, for discharge 154366, similar to 154406 of figures 1–3, but without ECCD. The figure shows that both with and without E × B shear effects, neoclassical transport is the dominant mechanism for ion energy flux, and the turbulent ion energy fluxes are negligible inside $\rho < 0.7$. Both with and without E × B shear, the predicted ion profile (with boundary condition at $\rho = 0.8$) matches well the experimental profile, suggesting that turbulence suppression mechanisms other than E × B effect may play a major role in these discharges, such as Shafranov shift turbulence stabilization [23]. Notice that, in the prediction without E × B shear [figure 4(*e*)], the foot of the ITB has moved slightly inward. It is not clear whether this small effect would be significant enough to cause progressive shrinking of the ITB radius, nevertheless it is consistent with the speculation by Tala *et al* [18] discussed above. However, analysis of the E × B shear components in these plasmas suggests that the E × B shear affecting the ITB foot can be produced by the pressure gradient associated with the ITB itself,

and does not rely on externally driven large toroidal rotation shear. Figure 4(*g*) shows the E × B shearing rate from each component of the E × B rotation, $\omega_E = \frac{\partial P_C / \partial \psi}{6 n_C e} + \frac{V_\phi}{R} - \frac{B_\phi V_\theta}{R B_\theta}$. At the radii where the turbulent fluxes become significant, i.e. $\rho \sim 07$–0.8, the contributions to the E × B shearing rate from the poloidal rotation is negligible, while the contributions from toroidal rotation and pressure gradient are in competition leading to a total E × B shearing rate that is smaller than the contribution from the pressure gradient alone. Since the total E × B shearing rate is sufficient to quench the turbulence, the larger E × B shearing obtained without toroidal rotation should improve turbulence suppression at these radii. This is confirmed by the analysis shown in figures 4(*c*) and (*f*): by setting the E × B shearing rate in TGYRO equal to the term from the pressure gradient only, the turbulence is sufficiently suppressed that the inward shift in the ITB foot is removed and the predicted ion profile matches the experimental profile.

These transport analysis results may be consistent with the experimental observations, reported in [24] that sustained high q_{min} and excellent confinement are also observed in high-β_P discharges with NBI torque ~3 Nm, i.e. reduced by about a factor of two relative to all co-NBI operation (such as discharge 154406 in figures 1–3). One difficulty in comparing the low NBI torque and high NBI torque experiment results is a significant difference in the pedestal height. Planned future experiments to test the rotation dependence of the ITB should further investigate the pedestal height variation as the torque is varied, and should be able to reach NBI torque near zero, albeit giving up on the fully noninductive condition.

3. MHD stability limits and fast ion losses

Stability analysis shows that these high-β_P discharges operate against the MHD stability limit with an ideal wall at the position of the DIII-D wall. As an example, this section discusses equilibrium and stability analysis for discharge 154366, which maintains high $\beta_N \geqslant 3$ with small, infrequent relaxation oscillations (discussed in section 4). Figure 5 shows two kinetic equilibrium reconstructions for $t = 4.185$ s, shortly before a relaxation oscillation event. The cross section of plasma and conducting vessel shows the large plasma-wall gap at the outer midplane, of about ~14 cm. This should be compared with more routine DIII-D operation using an outer gap of 8–10 cm. As mentioned in section 2, in addition to the extensive set of measurements available for equilibrium reconstruction at DIII-D, these reconstructions use a bootstrap current model to further constrain the edge current density at minor radius $0.8 < \rho < 1$. The edge bootstrap current densities predicted by the Sauter model [13] and the first principle kinetic code NEO [12] are used as constraints (respectively solid and dashed lines in figure 5). For this discharge, the two models differ only slightly (about 10%), with the NEO bootstrap model yielding a slightly better fit of the experimental measurements. However, in cases with higher pedestal density, leading to higher collisionality, it was found [25] that the Sauter formula significantly over-predicts the bootstrap current, a finding that supports recent theoretical work by Belli
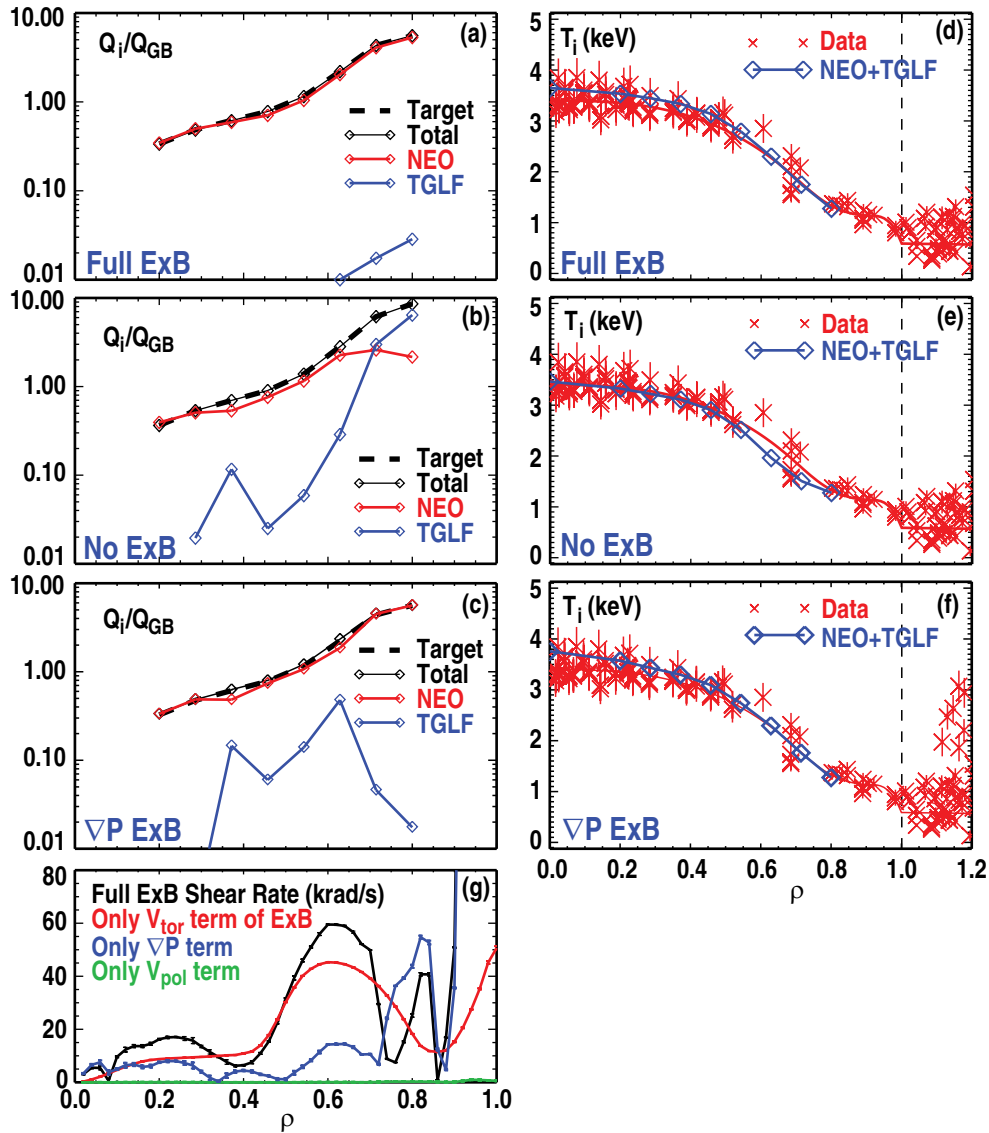
Figure 4. Steady-state TGYRO simulations of the ion temperature profile in discharge 154 366 at $t = 4.2$ s, with total experimental E × B shearing rate (*a*), (*d*), with zero E × B shearing rate (*b*), (*e*), and with only the diamagnetic term (pressure gradient) of the E × B shearing rate (*c*), (*f*). (*a*)–(*c*) Energy fluxes normalized to gyro-Bohm transport: target (experiment), total (predicted) and its turbulent (TGLF) and neoclassical (NEO) components. (*d*)–(*f*) Comparison of measured and predicted ion temperature profiles. (*g*) Experimental total E × B shearing rate and E × B shearing rate from each component of the E × B rotation: polodal, toroidal, and diamagnetic.

et al [26]. Stability of both equilibrium reconstructions (using Sauter and using NEO) is tested here in order to qualitatively estimate the impact of the uncertainty in the edge current profile determination.

Ideal MHD calculations of the $n = 1$ kink mode stability with an ideal wall approximating closely the shape of the DIII-D vessel are shown in figure 6 for the two reconstructions, using Sauter and NEO bootstrap current. The stability code allows us to vary the minor radius of the ideal wall, to test the effect of plasma-wall separation on the instability. For either reconstruction, the plasma is calculated to be at marginal stability with the ideal wall at the position of the DIII-D wall. The mode structure shows large internal components driven by the pressure gradients at the ITB. Nevertheless, this is an external mode that can be stabilized by a sufficiently close conducting wall.

Indeed, these experiments used a large plasma-wall gap to reduce wall heating by fast ion losses. At relatively low plasma current and large NBI power, the compound losses from classical (due to large orbits) and anomalous [due to Alfvén eigenmodes (AEs) and possibly other instabilities] effects can be significant and can lead to overheating and damage of the limiter tiles. However, recent detailed analysis [27] has shown that the anomalous fast ion losses are high mostly during the β_N and density ramp-up phase, i.e. when the NBI power has increased significantly but the density has not yet reached flattop. This understanding opened the possibility of developing an optimized waveform of the outer gap that could increase the ideal-wall limit without leading to unacceptable levels of wall over-heating. A summary of the fast ion loss analysis is shown in figure 7. The measured neutron rate and stored energy for discharge 154 406 are compared to
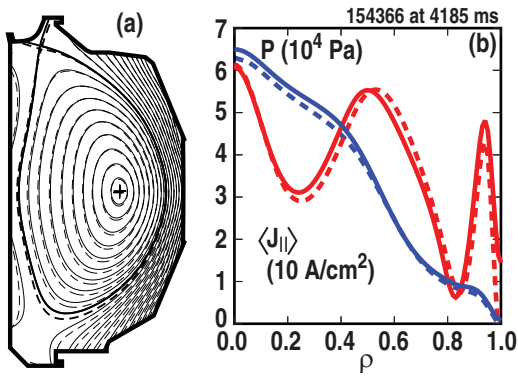
Figure 5. Equilibrium reconstructions for discharge 154 366 at $t = 4.185$ s. Solid (dashed) curves show results using the Sauter (NEO) model as edge current constraint. (*a*) Cross section of plasma and limiter wall. (*b*) Radial profiles of the plasma pressure and flux averaged parallel current density.
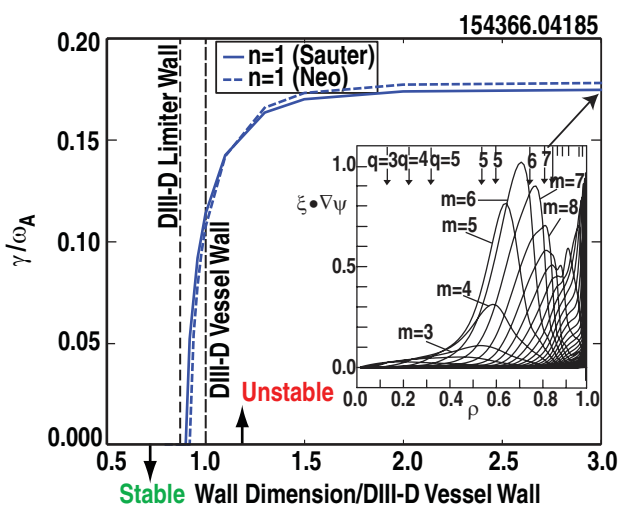

Figure 6. Calculated growth rate of the $n = 1$ ideal kink mode normalized to the Alfvén frequency versus the ideal wall radius multiplier relative to the DIII-D vessel wall for discharge 154 366 at $t = 4.185$ s (multiplier = 1 indicates an ideal wall at the position of the DIII-D wall). Solid (dashed) curve shows results for an equilibrium reconstruction using the Sauter (NEO) model as edge current constraint. Inset shows the mode structure for the ideal wall far away from the plasma.

TRANSP calculations using three different levels of beam ion diffusivity (DB = 0, 0.5, and 5.0 $m^2 s^{-1}$) as well as a temporally varying diffusivity. The variable diffusivity coefficient was derived by interpolating the results of the constant diffusivity runs to match the temporal evolution of the experimentally observed neutron rate. In all cases the beam ion diffusivity is constant in radius. Panel figure 7(*d*) shows that the required diffusivity changes significantly over time, and roughly tracks the AE mode activity visible in the spectra calculated from the CO_2 interferometer [figure 7(*a*)]. The time-varying anomalous fast ion losses may be understood as the result of the interplay between the AE activity and the plasma density. As the density increases, the fast ion slowing down time decreases, accomplishing two tasks: the fast ion content is reduced (thereby reducing the AE instability drive), and the fast ions displaced by the AE instabilities travel shorter
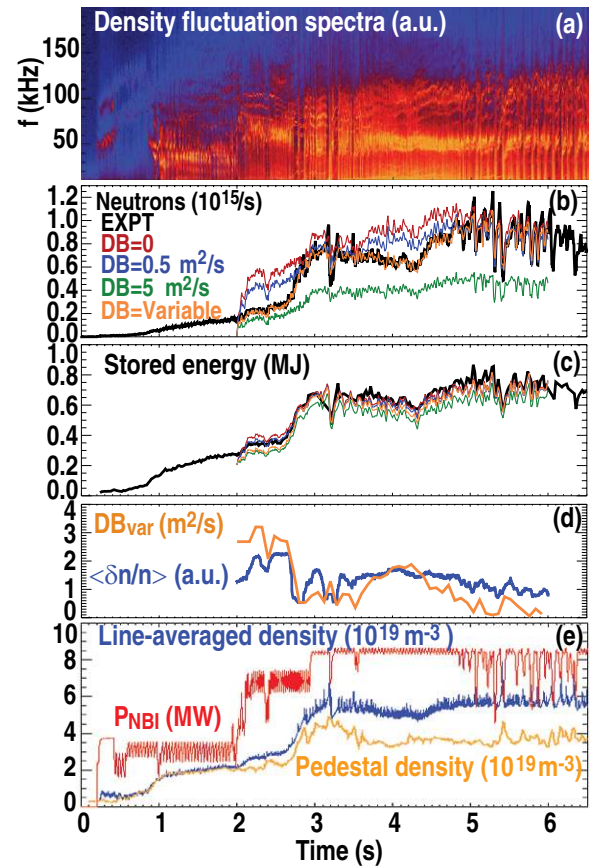

Figure 7. Time histories of: (*a*) combined frequency spectra of line-integrated density fluctuations from four separate CO_2 interferometer chords; (*b*) measured and calculated neutron rate (calculations are carried out using different values of the spatially-uniform beam-ion diffusion coefficient DB, color coded); (*c*) measured and calculated stored energy (same color code used for the neutron rate); (*d*) value of DB required to match the measured neutron rate, and integrated density fluctuation amplitude above 20 kHz, normalized to the line averaged density (20 kHz lower frequency chosen to eliminate vibration contribution to CO_2 phase fluctuations); (*e*) line averaged electron density, pedestal density, and NBI power.

distances prior to thermalization. Both effects lead to reduced fast ion losses. The pedestal density is particularly effective at slowing down the fast ions because of the relatively low temperature at large minor radius ($T_i \sim 0.5$ keV at $\rho \sim 0.95$). Once the density has reached a sufficiently high flattop, the inferred fast ion losses are reduced to near classical levels, despite the very high values of q_{min} which can be associated with stronger AE drive through coupling to higher order resonances [28]. In addition to the slowing down effect of the density discussed here, recent analysis with the Nova code [28] indicates that the Alfvén continuum in the core of these plasmas during the high density phase is relatively closed, which may also contribute to the reduced AE activity and resulting fast ion transport. These results are similar to the observations in [29, 30] that AE modes are stable in negative shear discharges with large density gradient at the ITB, although the regime under consideration here is significantly different, with a q-profile that is flatter in the core and overall significantly higher [see figure 3(*c*)].
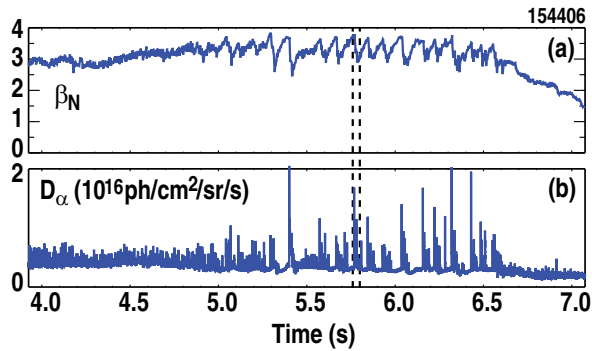
Figure 8. Time traces of β_N and D_α light, showing large ELMs and the relaxation oscillation effect on the stored energy. Vertical dashed lines show the time range expanded in figure 8.

4. Relaxation oscillations: edge localized modes (ELMs) and ITB

Similar to the earlier DIII-D experiments in the high-β_P regime [5], relaxation oscillations have been observed to limit the plasma performance in these new experiments as well. However, thanks to high time resolution measurements, here the oscillations are identified as the repetitive buildup and collapse of the H-mode pedestal, not the ITB. Usually, the ITB persists through the oscillations in stored energy, while the H-mode pedestal is significantly reduced. This section presents an example of this observations, together with evidence that the main cause of the relaxation oscillations is the coupling of ELMs with the marginally stable, ideal-wall $n = 1$ external kink mode. The implication of this hypothesis is that the relaxation oscillations could be ameliorated and the plasma performance improved by increasing the ideal-wall beta limit, for example by reducing the plasma-wall separation gap. This suggestion was tested in the experiments, and the successful results are also shown in this section.

Figure 8 shows the strong impact of the oscillations on the β_N waveform. Once β_N is pushed above a value of ~3, the ELMs become particularly large. Larger ELMs cause deeper excursions in the stored energy from which it takes longer to recover, and which often trip off one or more neutral beams by the sudden increase in base pressure near the beam ducts. In some cases, a large ELM is followed by a total collapse of the stored energy, and in a few cases even by a current disruption.

Figure 9 takes a detailed look into one of these stored energy oscillations, in the time range between vertical dashed lines in figure 8. The stored energy drop is caused by a rapid series of short bursts of an $n = 1$ mode. The time scales for growth/decay is ~100 μs, and the rotation is ~1 kHz [figure 9(d)]. The time evolution of the electron temperature profile in figures 9(a) and (e) shows that the consequence of these bursts is a large reduction of the edge temperature and a much smaller reduction of the core temperature, i.e. an abatement of the large H-mode pedestal and a slight inward movement of the ITB. The bursty $n = 1$ events appear to be relaxation instabilities driven by pedestal gradients and dominated by $n = 1$, rather than higher n as most ELMs are. The rapid decay could be a result of the mode reducing the driving gradient. The first

$n = 1$ burst usually has a shorter growth time (<100 μs), more localized spatial structure, and larger spike signature in the photo-diode D_α signal, all characteristics of an ELM. The following bursts have longer growth time ($\geqslant$200 μs) and more sinusoidal $n = 1$ spatial structure. This slower growth compared to a standard ELM is consistent with an $n = 1$ kink mode occurring at the ideal MHD stability limit, and is discussed later in this section.

Figure 10 shows the results of an experimental test of the ideal-wall limit effect, using a scan of the plasma-wall outer gap. The input for the two high-β_P discharges shown differs only in the programmed waveform for the plasma-wall outer gap. Discharge 159 206 with the larger gap (the previous standard for this low current regime) suffers a beta collapse and disruption at β_N ~ 3.6. Discharge 159 213 exceeds this β_N value, and sustains $\beta_N \leqslant 4$ until the high NBI power phase ends. This macroscopic demonstration of the wall stabilization effect provides support for the accuracy of the ideal MHD calculations of the ideal-wall stability limit presented in the previous section. Figures 10(e)–(g) show several plasma profiles (from measurements and equilibrium reconstruction) for discharge 159 213 at one time during the sustained high performance phase. An ITB at large minor radius is clearly visible in all channels (n_e, T_e, T_i rotation). About 93% of the total plasma kinetic energy is stored within the ITB foot at ρ ~ 0.75. Ideal MHD stability analysis shows that these profiles are $n = 1$ stable with an ideal wall at the position of the DIII-D vessel. Note that this discharge does not have ECCD, which (as mentioned in section 2) results in a steeper T_i ITB and a weaker T_e ITB compared to discharge 154 406 of figure 3. Also, cases without ECCD have larger core rotation for the same NBI torque. Also note that the temperature ITBs have their foot at slightly larger minor radius than discharge 154 406: ρ ~ 0.75 instead of ρ ~ 0.7. We speculate that this is due to the higher β values and thus larger Shafranov shift. A broad database analysis investigating the dependence of the ITB radius on the β values is in progress.

Key differences with other ITB experiments that reported reduced β_N limits because of a barrier localized $n = 1$ mode [31, 32] may be the larger plasma-wall separation in those early JT-60U experiments, and the smaller radius of the ITB in TFTR and JET. Both differences lead to the mode being farther away from a stabilizing wall. Also, the very large Shafranov shift in these DIII-D experiments contributes to place the dangerous ITB gradients closer to the stabilizing conducting wall.

In discharge 159 206, β_N reaches a value of about 3.6, or about 5 times the internal inductance l_i, at which point (t ~ 4830 ms) the plasma disrupts due to a rapidly growing instability. The instability is consistent with an $n = 1$ kink mode occurring at the ideal MHD stability limit. Just before the instability, data from the toroidal array of Mirnov loops show a large, single filament-like pulse that grows and decays in about 200 μs, while making almost two toroidal rotations. This is a typical magnetic signature of an ELM. The large ELM leads directly into the $n = 1$ mode growing to large amplitude (~60 G) with a rotation frequency $w/2\pi$ ~ 1 kHz and a growth time of τ_g ~ 250 μs (figure 11).
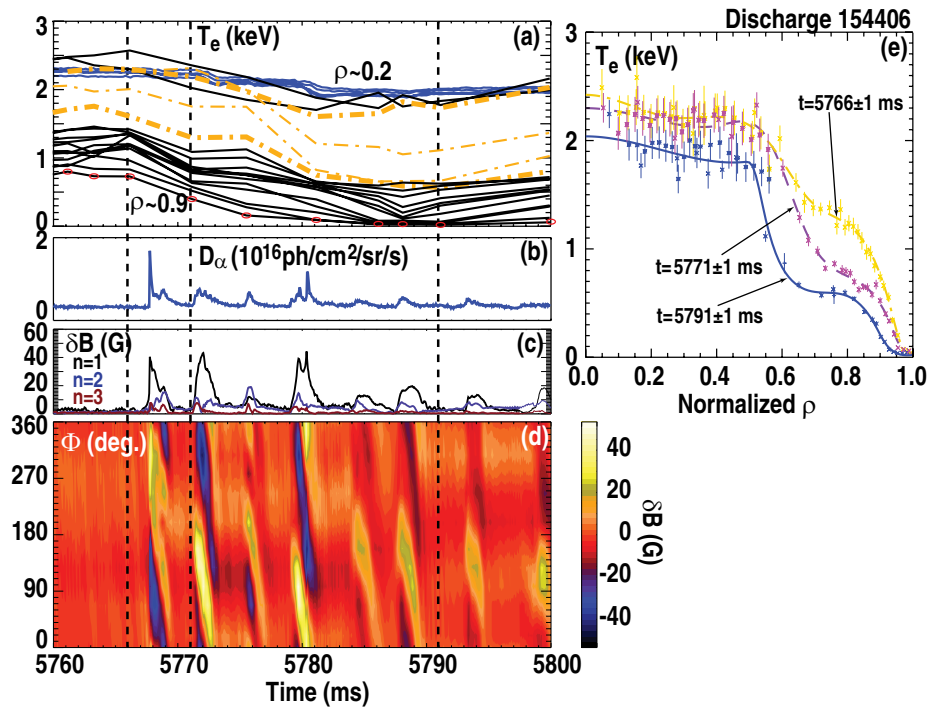
Figure 9. Time evolution of (*a*) electron temperature measured by Thomson scattering at $0.2 \leqslant \rho \leqslant 0.9$, and by electron cyclotrom emission (ECE) at $0.2 \leqslant \rho \leqslant 0.3$; (*b*) D_α light; (*c*) $n = 1, 2$, and 3 components of the perturbed magnetic field at the outer midplane measured by poloidal field sensors. (*d*) Color coded contour plot of the perturbed poloidal field versus time and toroidal angle. (*e*) Radial profiles of the electron temperature at times indicated by vertical dashed lines.
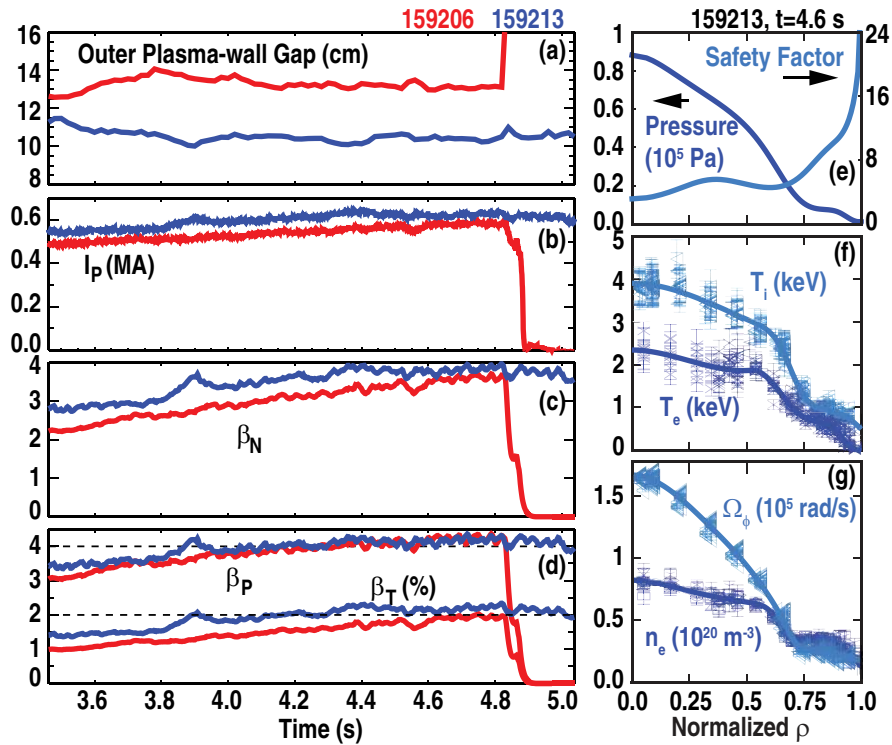

Figure 10. (*a*)–(*d*) Time traces of selected plasma parameters for similar discharges with only input difference in the plasma-wall outer gap. (*e*)–(*g*) Radial profiles for discharge 159 312 at $t = 4.6$ s, showing ITBs at $\rho \sim 0.7 - 0.75$.

While the large $n = 1$ mode is the ultimate disruption cause, the immediately preceding ELM is a particularly large one, probably because its low n components are amplified by proximity to the global ideal-wall stability limit. Both the measured growth time and the rotation frequency of the $n = 1$ mode, are consistent with previous observations of $n = 1$ kink mode near the ideal-wall stability limit on DIII-D [6]. The growth time can be understood from a model [33] of an ideal mode slowly
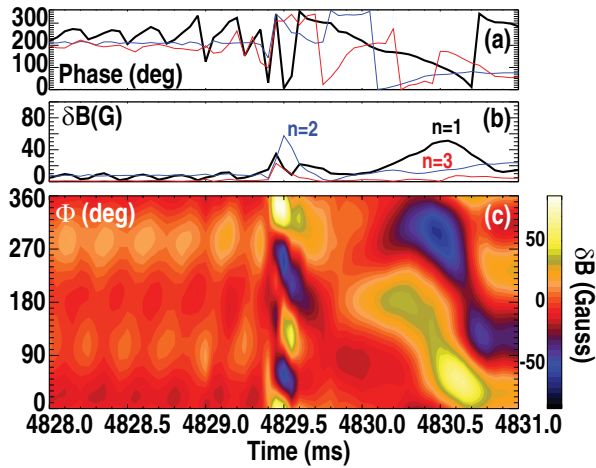
Figure 11. Analysis of perturbed poloidal field measurements in discharge 159 206 at times just before the disruption.

Figure 12. Scatter plots of β_N/l_i, β_N, β_P, and β_T versus the plasma wall separation at the outboard midplane, for a database comprising the last 20 discharges of high β_P experiments analyzed between $t = 2$ s and $t = 6$ s. Panel (*b*) include the calculated $n = 1$ ideal-wall limit for one representative high-β_P discharge versus the outer plasma wall separation.

driven through the stability boundary: $\tau_g = \tau_{MHD}^{2/3}\tau_h^{1/3}$, where τ_{MHD} is of the order of the expected growth time of the ideal MHD mode and τ_h is the time scale for the increase of the instability drive. For a global kink-ballooning mode, the instability drive is provided by both high plasma pressure (high β_N) and high current density near the plasma edge (low l_i). Therefore the instability drive in this case is proportional to the ratio β_N/l_i. Here, l_i is nearly constant while β_N is ramping up with a rise time $\tau_h \sim 0.6$s, which, with the measured growth time of the kink mode, yield $\tau_{MHD} \sim 5\mu s$. This time is indeed consistent with expectations for ideal MHD instabilities. Therefore, the experimentally observed growth time of ~260 μs is consistent with an ideal kink mode slowly driven through the ideal-wall limit.

Further optimization of the scenario waveforms has led to additional improvements in the achievable plasma performance, with maximum β_N up to 4.3, β_N up to 4.5, β_T up to 3%, and ratio β_N/l_i up to >8. The scatter plots in figure 12 are from a database comprising the last 20 discharges of these experiments. A clear trend is observed, with both wall stabilization, measured by the ratio β_N/l_i, and absolute performance, measured by either β_N, or β_P, or β_T, strongly improving with reduced outer gap. The maximum values of β_N/l_i and of β_P are among the highest ever observed on DIII-D. It is particularly remarkable that these record values are achieved in plasmas with ITBs. These results are a clear demonstration that ITB plasmas are compatible with high beta limits, as long as the ITB is at large minor radius and the conducting wall is sufficiently close to the plasma, yielding a strong coupling between the kink mode and the wall.

Figure 12(*b*), also shows the ideal-wall β_N limit calculated against the $n = 1$ ideal MHD kink mode with varying outer gap. The β_N limit is calculated from the experimental reconstruction of one high-β_P discharge at $\beta_N \sim 3$. To find the maximum stable β_N for each wall position, a series of plasmas with increasing β_N is generated using EFIT by scaling the experimental pressure profile while keeping the q-profile constant (as much as possible). The ideal-wall β_N limit dependence
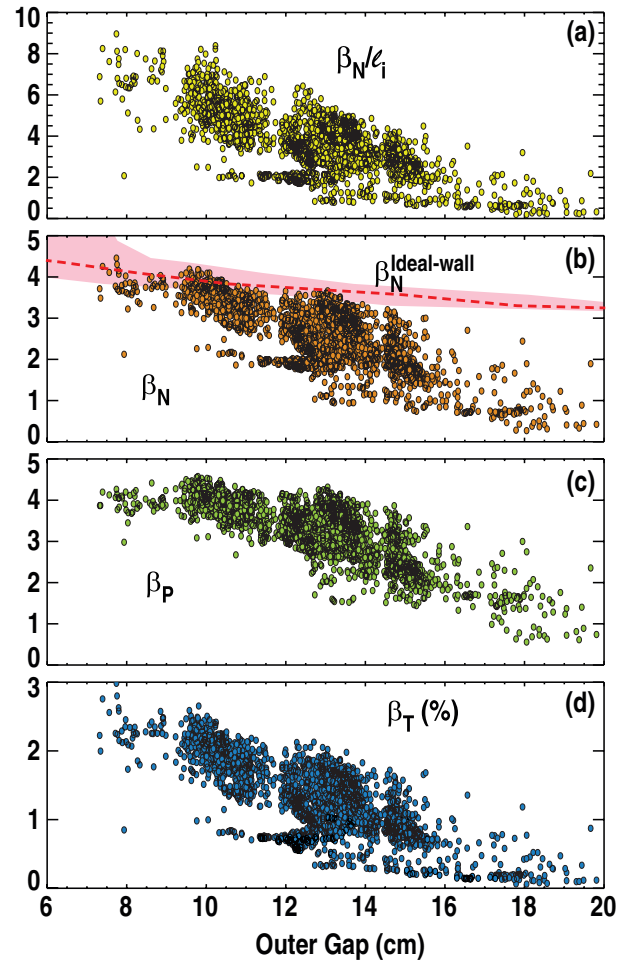
on the outer gap seems to correctly capture the trend of the maximum experimentally achieved β_N.

5. Summary and conclusions

Recent DIII-D experiments have increased confidence in the potential of the high bootstrap fraction approach for applicability to a steady state fusion reactor. These experiments were largely motivated by the interest in the developing and testing a possible scenario for steady-state advanced tokamak demonstration on EAST. Fully noninductive plasmas have been sustained for long durations with bootstrap fraction $f_{BS} \geqslant 80\%$, $\beta_N \leqslant 4$, $\beta_P \geqslant 4$, and with $\beta_T \geqslant 2\%$, and with excellent energy confinement quality, with $H_{98y,2} \sim 1.5$. The excellent confinement is associated with the formation of an ITB at large minor radius in all channels (n_e, T_e, T_i rotation). Transport analysis and preliminary experimental results suggest that, in this high-β_P regime, the toroidal rotation shear does not contribute significantly to sustainment of the ITB at large minor radius and good bootstrap
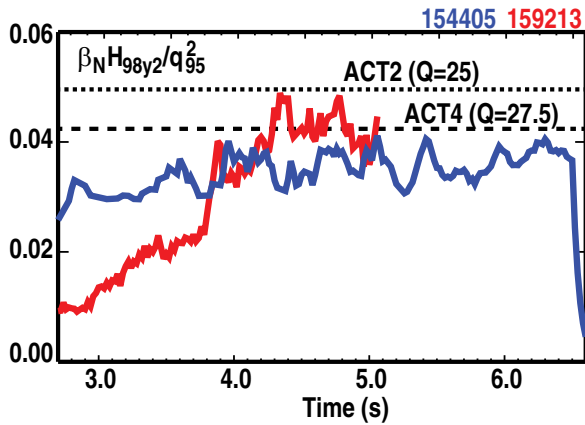
Figure 13. Time traces of the normalized fusion performance parameter G = $\beta_N H_{98y,2}/q_{95}^2$ for discharges 159 213 (red trace) and 154 405 (blue trace), compared to the target values of G for ARIES-ACT2 ($\beta_N = 2.6$, $H_{98y2} = 1.22$, $q_{95} = 8$, and plasma fusion gain $Q = 25$) and ARIES-ACT4 ($\beta_N = 2.47$, $H_{98y2} = 1.24$, $q_{95} = 8$, and Q=27.5, using more advanced engineering).

current alignment. If confirmed by further experiments, this would be a very important result for the applicability of this regime to a fusion reactor, where the toroidal rotation is not expected to be large.

Another important result, showing robust stability without external control, is that the ITB is maintained at large minor radius despite ELM perturbations, which become particularly large as β_N is pushed against the global ideal-wall limit. The transient stored energy drops caused by these coupled edge-core modes have been previously referred to as 'relaxation oscillations'. The maximum achievable β_N is limited by the stability of these modes, and depends on the plasma-wall separation, which is in turn dictated by the operational need to reduce wall heating by fast ion losses, which can be large in the high β_P regime of low plasma current. During the course of these experiments, it was found that the fast ion losses are unacceptably high only during the β_N and density ramp-up phase, i.e. when the NBI power has increased significantly but the density has not yet reached flattop. This understanding led to the development of an optimized waveform of the outer gap, consisting of large outer gap until high density is established and reduced outer gap afterwards, thus increasing the ideal-wall limit during the high β_N phase, without leading to unacceptable levels of wall heating. Using this optimized outer gap waveform has enabled a significant (~30%) performance increase relative to earlier work, demonstrating that ITB plasmas can be compatible with high beta limits, and has opened the path to future performance improvements. For example, with access to higher β_N it should be possible to maintain fully noninductive conditions at higher levels of plasma current, and thus higher β_T.

Furthermore, note that the levels of normalized plasma performance already achieved and sustained fully noninductively ($\beta_N \sim \beta_P \sim 4$, $\beta_T \sim 2\%$), significantly exceed those envisioned in recent ARIES-ACT steady-state fusion reactor studies ($\beta_N \sim \beta_P \sim 2.5$, $\beta_T \sim 1.5\%$) [34]. The large values of β_N and energy confinement quality achieved in these experiments

compensate for the low plasma current relative to the magnetic field, i.e. the high q_{95} values. More quantitatively, the fusion performance can be evaluated using the normalized fusion performance parameter $G = \beta_N H_{98y,2}/q_{95}^2$ [35]. Figure 13 shows the time trace of G for discharge 159 213 of figure 9 and discharge 154 405 (similar to 154 406 of figures 1–3), compared to the target values of *G* for ARIES-ACT2 and ARIES-ACT4. Despite the large values of q_{95} ~10–12 in these DIII-D experiments, the normalized fusion performance achieved fully noninductively is comparable to that envisioned for the ARIES-ACT2 and ARIES-ACT4 fusion DEMO concepts.

Acknowledgment

References

[1] Wan B. *et al* 2014 *Proc. of 41st EPS Conf. on Plasma Physics* (*Berlin, Germany, 23–27 June 2014*) vol 38F http://ocs.ciemat.es/EPS2014PAP/pdf/O2.104.pdf
[2] Fujita T. *et al* 2002 *Nucl. Fusion* **42** 180
[3] Sakamoto Y. *et al* 2005 *Nucl. Fusion* **45** 574
[4] Sakamoto Y. *et al* 2009 *Nucl. Fusion* **49** 095017
[5] Politzer P.A. *et al* 2005 *Nucl. Fusion* **45** 417
[6] Garofalo A.M. *et al* 2002 *Phys. Rev. Lett.* **89** 235001
[7] Takechi M. *et al* 2007 *Phys. Rev. Lett.* **98** 055002
[8] Bizarro J.P.S., Litadon X., Tala T.J.J. and JET EFDA Contributors 2007 *Nucl. Fusion* **47** L41
[9] Hawryluk R.J. 1980 An empirical approach to Tokamak transport *Physics of Plasmas Close to Thermonuclear Conditions* ed B Coppi *et al* (Brussels: CEC) vol 1 p 19
[10] Mikkelsen D.R. 1989 *Phys. Fluids* B **1** 333
[11] Lao L.L. *et al* 1985 *Nucl. Fusion* **25** 1611
[12] Belli E.A. and Candy J. 2012 *Plasma Phys. Control. Fusion* **54** 015015
[13] Sauter O., Angioni C and Lin-Liu Y.R. 2002 *Phys. Plasmas* **9** 5140
[14] Fujita T. *et al* 1999 *Nucl. Fusion* **39** 1627
[15] Houlberg W.A. *et al* 2005 *Nucl. Fusion* **45** 1309
[16] Koide Y. *et al* 1994 *Phys. Rev. Lett.* **72** 3662
[17] Sips A.C.C. *et al* 1998 *Plasma Phys. Control. Fusion* **40** 647
[18] Tala T.J.J. *et al* 2001 *Plasma Phys. Control. Fusion* **43** 507–23
[19] Candy J. *et al* 2009 *Phys. Plasmas* **16** 060704
[20] Staebler G.M., Kinsey J.E. and Waltz R.E. 2005 *Phys. Plasmas* **12** 102508
[21] Kinsey J.E., Staebler G.M. and Waltz R.E. 2008 *Phys. Plasmas* **15** 055908
[22] Candy J. and Waltz R.E. 2003 *J. Comput. Phys.* **186** 545

[23] Beer M.A., Hammett G.W., Rewoldt G., Synakowski E.J., Zarnstorff M.C. and Dorland W. 1997 *Phys. Plasmas* **4** 1792

[24] Gong X. *et al* 2014 Development of fully noninductive scenario at high bootstrap current fraction for steady-state Tokamak operation on EAST and DIII-Daper *presented at the IAEA Int. Conf. on Fusion Energy* (*St Petersburg, Russia, 13–18 October 2014*)

[25] Ren Q. *et al* 2015 *Plasma Phys. Control. Fusion* **57** 025020

[26] Belli E.A., Candy J., Meneghini O. and Osborne T.H. 2014 *Plasma Phys. Control. Fusion* **56** 045006

[27] Heidbrink W.W. *et al* 2014 *Plasma Phys. Control. Fusion* **56** 095030

[28] Holcomb C.T. *et al* 2015 *Phys. Plasmas* **22** 055904

[29] Kimura H. *et al* 1998 *Nucl. Fusion* **38** 1303

[30] Kusama Y. *et al* 1999 *Nucl. Fusion* **39** 1837

[31] Manickam J. *et al* 1999 *Nucl. Fusion* **39** 1819

[32] Baranov Y.F. *et al* 2012 *Nucl. Fusion* **52** 023018

[33] Callen J.D., Hegna C.C., Rice B.W., Strait E.J. and Turnbull A.D. 1999 *Phys. Plasmas* **6** 2963

[34] Kessel C.E. *et al* 2015 *Fusion Sci. Technol.* **67** 1

[35] Luce T.C. *et al* 2004 *Phys. Plasmas* **11** 2627